Aeolian silt transport processes as fingerprinted by dynamic image analysis of the grain size and shape characteristics of Chinese loess and Red Clay deposits

Shang, Yuan; Kaakinen, Anu; Beets, Christiaan J.; Prins, Maarten A.

published in
Sedimentary Geology
2018

DOI (link to publisher)
10.1016/j.sedgeo.2017.12.001

document version
Publisher's PDF, also known as Version of record

Sedimentary Geology 375 (2018) 36–48

Contents lists available at ScienceDirect

Sedimentary Geology

journal homepage: www.elsevier.com/locate/sedgeo

Special Issue Contribution: ANALYSIS OF SEDIMENT PROPERTIES AND PROVENANCE

Aeolian silt transport processes as fingerprinted by dynamic image analysis of the grain size and shape characteristics of Chinese loess and Red Clay deposits

Yuan Shang [a,b,*], Anu Kaakinen [a], Christiaan J. Beets [b], Maarten A. Prins [b,**]

[a] Department of Geosciences and Geography, P.O. Box 64, 00014, University of Helsinki, Finland
[b] Department of Earth Sciences, Faculty of Science, Vrije Universiteit Amsterdam, De Boelelaan 1085, 1081 HV Amsterdam, The Netherlands

ARTICLE INFO

Article history:
Received 22 August 2017
Received in revised form 27 November 2017
Accepted 3 December 2017
Available online 7 December 2017

Keywords:
Aeolian dust
Dynamic image analysis
Aspect ratio
Particle size and shape sorting
Chinese Loess Plateau

ABSTRACT

This study applied dynamic image analysis (DIA; Sympatec Qicpic) to characterize the grain size and shape of Chinese aeolian sediments in order to fingerprint their transportation processes. This is the first time this technique has been applied to late Neogene and Quaternary silt particles (2–63 μm) from the Chinese Loess Plateau (CLP). We selected four well-studied Quaternary loess-palaeosol sequences along a north-south transect across the CLP and compared their grain size distribution obtained by DIA with that yielded by laser diffraction particle size analysis (LD; Fritsch Analysette 22 and Sympatec HELOS KR). This comparison demonstrated that DIA is successfully able to differentiate loess units from palaeosols, and to characterize clearly spatiotemporal variations in the grain size records of loess-palaeosol sequences formed during the last two glacial and interglacial periods. This is consistent with grain size results obtained using LD. DIA is also able to characterize spatial variations in the more fine-grained aeolian Red Clay deposits underlying the Quaternary loess, and allows the quantification of the fluvial contribution to Red Clay sequences. DIA of the characteristics of grain shapes in loess-palaeosol sequences and Red Clay deposits revealed a systematic pattern, whereby the aspect ratio decreased with increasing grain size, indicating that systematic shape sorting occurred during the aeolian transportation of these dust particles. It could be inferred from our study that particles in a certain grain size range correspond to a specific aspect ratio range, and may in turn be aerodynamically distinguishable from each other and further correlated with the wind velocity/strength. Also evident from analysis of our DIA data was a subtle but systematic downwind decrease in the aspect ratio of the particles in the loess units. This observation suggests that elongated and/or flat particles (with a low aspect ratio) were transported further downwind than more symmetrically shaped particles (with a high aspect ratio). This study indicates that DIA of grain size and shape characteristics can be an additional powerful tool for identifying grain size and shape sorting trends, determining the dominant mode of transport, and reconstructing transport pathways of silt-sized aeolian sediments.

1. Introduction

Grain size as a fundamental property of sedimentary particles has been extensively used to characterize the sedimentary environment and transport mechanisms of natural sediments (Udden, 1914; Wentworth, 1922; Folk and Ward, 1957; Visher, 1969; Mclaren and Bowles, 1985; Rea and Hovan, 1995; Syvitski, 1997; Prins and Weltje, 1999; Vandenberghe, 2013). Various techniques have been developed to determine the grain size of sediments, including classical methods such as microscope particle sizing, sieving, settling velocity measurements, as well as automatized techniques such as photon correlation spectroscopy and laser diffraction (LD) particle size analysis (Syvitski, 1997). Of these techniques, LD particle analyzers are increasingly used because of their high accuracy, fast speed, and low cost in processing large numbers of samples (Konert and Vandenberghe, 1997; Eshel et al., 2004; Blott and Pye, 2006; Fedotov et al., 2007; Jonkers et al., 2009, 2015).

Grain shape is another principal property of natural sediments that has been widely used in understanding the formation of the particles and in characterizing the transportation processes experienced by sediments (Wadell, 1932, 1935; Krumbein, 1941; Riley, 1941; Howard, 1992; Oakey et al., 2005; Blott and Pye, 2008; Suzuki et al., 2015). Many efforts have therefore been made to optimize particle shape analysis over the years. In early attempts at such analysis, particle shape was

* Correspondence to: Y. Shang, Department of Geosciences and Geography, P.O. Box 64, 00014, University of Helsinki, Finland.
** Corresponding author.
E-mail addresses: yuan.shang@helsinki.fi (Y. Shang), m.a.prins@vu.nl (M.A. Prins).

https://doi.org/10.1016/j.sedgeo.2017.12.001
0037-0738/

often manually characterized by using visual comparison diagrams based on the measurements of two-dimensional (2D) combined axis ratios (Krumbein, 1941; Sneed and Folk, 1958; Blott and Pye, 2008). Subsequently, computer-based image analysis has become more widely used, as it often measures the particles faster and more objectively than can manual methods (Persson, 1998; Kwan et al., 1999; Altuhafi et al., 2013; Rodriguez et al., 2013). However, in most cases, traditional static image analysis requires extended subsequent statistical analysis. In addition, many of the particle shape measurement techniques focus on coarse-grained material, such as sand and gravel-sized sedimentary particles.

In this study, we introduce a state-of-the-art technique, *i.e.* dynamic image analysis (DIA), which allows the rapid characterization of both the particle size and shape of silt and sand-sized clastic sediments. The setup used here (Sympatec Qicpic) combines a wet disperser with a high-speed image sensor (Qicpic), enabling the acquisition of a large number of images (several 10^3), and the analysis of a large number ($>10^4$ to $>10^6$) of suspended sedimentary particles in just a few minutes. Thus, it theoretically overcomes the problem inherited from traditional static image analysis of a limited number of image results with low particle counts and large statistical errors. The same DIA Qicpic technique has already been employed for measuring the grain size and shape of pharmaceutical materials (Yu and Hancock, 2008; Nalluri et al., 2010; Yu et al., 2011). However, only a few studies have so far exploited DIA methods in studying sedimentary characteristics, particularly for silt-sized particles (Tysmans et al., 2006, 2009; Li et al., 2015). Tysmans et al. (2009) applied automated dynamic image analysis (ADIA) (RapidVue Particle Analyzer, Beckman Coulter Company) to characterize the particle size and shape of Belgian loess, which is composed of >60% silt particles (2–63 μm). Their results have indicated that combining both grain size and shape can be very useful when reconstructing aeolian transportation processes, and can also discriminate loess deposits transported by different wind strengths and under differing climatic conditions (Tysmans et al., 2009). Li et al. (2015) used DIA (Qicpic) to examine the grain size and shape characteristics of lakeshore sands of Lake Tangra Yumco on the Tibetan Plateau (TP), and fluvial sands from the middle reaches of the Yellow River, Inner Mongolia. Both groups of sediments were deposited during the Holocene and are mainly composed of medium-grained (250–500 μm) and fine-grained (125–250 μm) sand. Their results demonstrated that for the sediments from both the TP lakeshore and the Yellow River floodplain, the mean grain size decreased as a function of increased sphericity. In addition, their results indicated that the lakeshore and alluvial sediments could be discriminated based on a combination of grain size and shape characteristics. Li et al. (2015) therefore suggested that this method could be a potentially useful tool in the reconstruction of sedimentary environments.

Here we applied the DIA method to characterize the grain size and shape of two distinct units of dust deposits on the CLP in northern China: Quaternary loess-palaeosol sequences; and the underlying late Miocene-Pliocene Red Clay. Loess is an aeolian sediment dominated by silt-sized particles; the loess-palaeosol records from northern China have been considered one of the most important continuous terrestrial archives of Quaternary climate change and atmospheric circulation (Liu, 1985; Kukla, 1987; Hovan et al., 1989; Pye, 1995; Liu and Ding, 1998; Porter, 2001; Muhs, 2013). The loess-palaeosol sequences on the CLP have been well studied from various perspectives, and it has been widely agreed that loess is a windblown product. Meanwhile, although there is a consensus on the aeolian origins of the upper part of the Red Clay sequence (~6–2 Ma BP) (Ding et al., 1998; An et al., 2001; Lu et al., 2001; Guo et al., 2002), debate still continues about whether the Red Clay sequence older than ~6 Ma BP is largely of aeolian origin, or was reworked by fluvial processes (Guo et al., 2001; Alonso-Zarza et al., 2009; Zhang et al., 2013; Nie et al., 2016; Shang et al., 2016). Therefore, the two objectives of this study were to: (1) examine the performance of DIA on silt-sized aeolian dust particles from loess-palaeosol sequences; and (2) compare the grain size and grain shape distributions of the Red Clay with loess and palaeosol samples to check the potential aeolian origins of the Red Clay.

2. Material and methods

2.1. Loess and Red Clay sections

The locations of the studied loess and Red Clay sections are indicated in Fig. 1. We selected four loess sections, referred to as Huanxian (HX), Xifeng (XF), Xunyi (XY) and Duanjiapo (DJP), along a north-to-south-oriented transect across the CLP. Detailed descriptions and age models of the sections were taken from Nugteren and Vandenberghe (2004) and Prins and Vriend (2007).The HX, XF and XY sections cover the last two glacial and interglacial cycles and contain (L0-) S0-L1-S1-L2-S2 loess (L)-palaeosol (S) units (Fig. 2). The studied DJP section only covers the last glacial and Holocene period (L0-S0-L1). In general, the Holocene palaeosol S0 and loess L0 correlate with Marine Isotope Stage 1 (MIS 1, 14–0 ka BP). The L1 loess was deposited during the Last Glacial (MIS 2-MIS 4, 71–14 ka BP), and contains two primary loess units, L1-1 and L1-3, and one weakly developed palaeosol complex (L1-2). Loess layer L2 was deposited during the penultimate glacial period and corresponds to MIS 6 (191–130 ka BP). L2 also consists of three sub-units marked as L2-1, L2-2 and L2-3 (Fig. 2). Similarly to L1-2, sub-unit L2-2 also represents a poorly-developed palaeosol (PDS) layer within the glacial loess unit L2, formed during interstadial periods. Note that the loess sub-units L1-1 (L2-1), L1-2 (L2-2) and L1-3 (L2-3) labeled in this study correspond to the nominations L1LL1 (L2LL1), L1SS1 (L2SS1) and L1LL2 (L2LL2), respectively, as used in previous studies (Hovan et al., 1989; Porter, 2001). The well-developed palaeosol complexes (WDS) S1 and S2 accumulated and formed during the last interglacial and penultimate interglacial periods, correlative with MIS 5 (71–130 ka BP) and MIS 7 (~191–243 ka BP), respectively (Nugteren and Vandenberghe, 2004; Prins and Vriend, 2007). The MIS ages are taken from Lisiecki and Raymo (2005, http://www.lorraine-lisiecki.com/LR04_MISboundaries.txt).

Samples for DIA (Sympatec QICPIC) and additional laser diffraction (LD) analysis (Sympatec HELOS) were selected based on variations in the median grain size and the proportional endmember records of the four studied loess sections (Fig. 2). The correlative samples taken from the same 'time slices' (stratigraphic intervals) are representative of typical loess (L) units (high median grain size (MD)/high proportion of EM1 and/or EM2), poorly-developed palaeosol (PDS) units, and well-developed palaeosol (WDS) units (low MD/high proportions of EM3) (Fig. 2 and Supplementary Table S1).

We also analyzed samples from three well-known Red Clay sections distributed across the CLP (Fig. 1): Baode (BD) on the northeastern CLP (Kaakinen et al., 2013); Lantian (LT) on the southern CLP (Kaakinen and Lunkka, 2003; Zhang et al., 2013); and Dongwan (DW) on the western CLP (Hao and Guo, 2004). The depositional ages of these sections span ~7.3–2.6 Ma BP and represent a variety of Red Clay lithologies (Supplementary Fig. S1). The BD Red Clay from the northeastern CLP is composed of two Red Clay formations, the late Miocene Baode (BD) Fm and the Pliocene Jingle (JL) Fm. The BD Fm has been partly affected by fluvial processes, whereas the JL Fm is composed of fine-grained wind-blown deposits (Kaakinen et al., 2013; Shang et al., 2016). The DW Red Clay sequence represents the uniform loessic Red Clays found on the western CLP (Hao and Guo, 2004), while the LT Red Clay (Lantian (LT) Fm) represents the southernmost occurrence of Red Clays, and is characterized by deep-red fine-grained deposits with fluvial components in the lowermost part of the sequence (Kaakinen and Lunkka, 2003; Zhang et al., 2013). Samples were selected based on their lithological characteristics and proportional variations within the modeled endmembers (a high proportion of EM1/EM2 *versus* a high proportion of EM3/EM4) for each Red Clay section

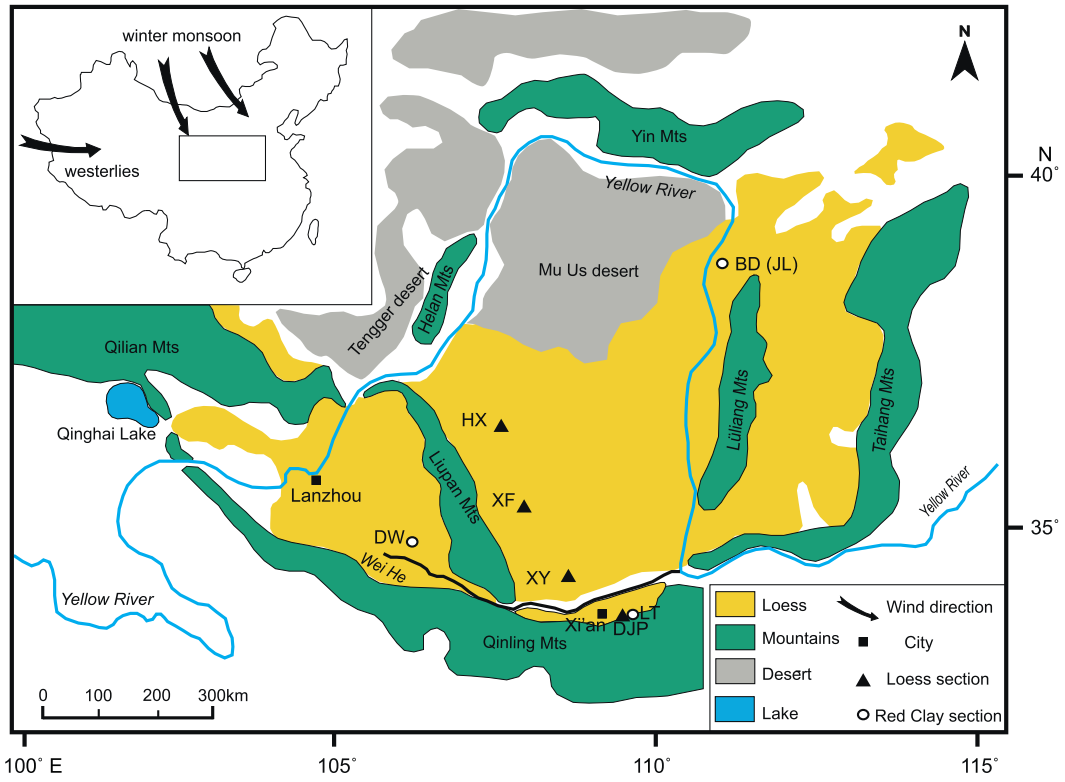

Fig. 1. The Chinese Loess Plateau (CLP) and locations of the studied loess and Red Clay sections. (Modified from Prins and Vriend, 2007).

(Shang et al., 2016). In particular, the samples with a high contribution of EM1 and/or EM2 were chosen to highlight the proportion of silt and sand particles found in fine Red Clay sediments (Supplementary Fig. S1). For the LT Red Clay, a few samples were selected from the intensively weathered upper part of the section, and two from the lowermost coarse-grained part, in order to investigate the influence of chemical weathering and fluvial processes on the particular characteristics observed in the distribution of grain size and shape within the sedimentary strata.

2.2. Laser-diffraction grain size analysis and data treatment

For grain size analysis, ~0.5–1 g of bulk sediment was pretreated with H_2O_2 and HCl to remove organic matter and carbonates, respectively, following a standard analytical procedure for loess and Red Clay (*cf.* Konert and Vandenberghe, 1997; Vandenberghe et al., 2004). The detailed loess grain size records (Fig. 2) and the LT Red Clay section (Supplementary Fig. S1) were obtained using a Fritsch A22 laser-diffraction instrument at Vrije Universiteit Amsterdam (VUA). Red

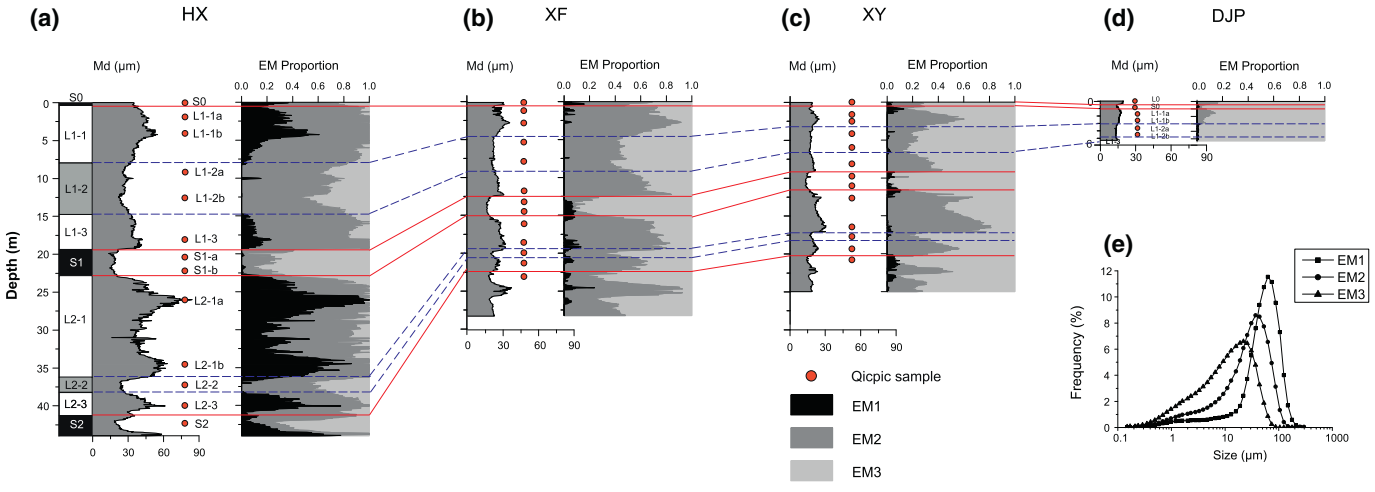

Fig. 2. Loess-palaeosol stratigraphy, median grain size (MD), and the proportional contributions of endmembers observed in the Huanxian (HX), Xifeng (XF), Xunyi (XY) and Duanjiapo (DJP) sections. The inset (e) shows the modeled endmember distributions (from Prins and Vriend, 2007). The grain size and endmember modeling data (all obtained using a Fritsch A22 laser diffraction (LD) particle size analyzer) are taken from Prins and Vriend (2007) and references therein; the grain size and EM-proportion records of the DJP section and the L2-S2 units of the HX, XF and XY sections are shown here for the first time. The red dots mark the levels sampled for DIA (Sympatec Qicpic) and additional LD particle size analysis (Sympatec HELOS).

Clay samples from the BD Fm were analyzed using a Coulter LS200, and from the JL Fm (BD) and from DW using a Sympatecs Helos KR laser diffraction particle sizer (Supplementary Fig. S1). A selected number of loess samples (indicated in Fig. 2) analyzed using Fritsch LD were reanalyzed with a Sympatec Helos KR LD particle sizer in order to make a comparison between different laser-diffraction devices and different techniques (LD *versus* DIA). Both LD devices produced grain size distributions with 56 size intervals within the size range 0.15–2000 μm (based on the parameter-free Fraunhofer model). The median grain sizes of the samples were calculated using the GRADISTAT program developed by Blott and Pye (2001).

Mixing models of these grain size distributions were produced to facilitate the collation of a total grain size dataset of the four loess sections (HX, XF, XY and DJP) using the End-Member Modeling Algorithm EMMA (Weltje, 1997). EMMA is a non-parametric numerical-statistical technique and its advantage over the parametric curve fitting approaches, *e.g.* Weibull (Sun et al., 2002, 2004) or log-normal (Xiao et al., 2009, 2013) is that it does not require any prior knowledge about the grain size controlling processes (Weltje and Prins, 2007). This method has proven to be powerful in distinguishing aeolian from fluvial sediments in various marine settings (*e.g.* Prins and Weltje, 1999; Prins et al., 2000; Stuut et al., 2002, 2014; Deplazes et al., 2014) and in portioning multiple transport/deposition processes of Quaternary loess (Prins and Vriend, 2007; Prins et al., 2007, 2009; Vriend et al., 2011). The endmember modeling results for the upper parts of these sections (S0-L1-S1) have already been published by Prins and Vriend (2007) and Prins et al. (2007), but the data for the L2-S2 units are reported here for the first time. The endmember modeling results for the Red Clay sections were taken from Shang et al. (2016).

2.3. DIA

A Sympatec image analysis sensor Qicpic/R connected to a LIXELL wet disperser (http://www.sympatec.com/EN/ImageAnalysis/QICPIC.html) was used to analyze various particle size and shape parameters of the loess and Red Clay samples. The Qicpic setup used in this study allows the analysis of as many as several million particles within the 2–500 μm range over a measuring time of 5 min. The pretreatment procedure for the DIA samples is similar to that for samples subjected to LD grain size analysis, and ensures that the samples are well dispersed during measurement.

The primary information given by the DIA is the contour (2D image) of any one particle (Fig. 3), which contains information about both the particle's size and shape. Standard size descriptors include the EQPC diameter, *i.e.* the diameter of the equivalent projection area of a circle, and the minimal, maximal and mean Feret diameters. However, it should be noted that the perimeter of the EQPC diameter of a (partly) transparent particle underestimates the 'true' diameter of that particle (Supplementary Fig. S2 and Table S2); the mean Feret diameter is therefore used here to describe the size of particles. The Feret diameter is based on a group of diameters derived from the distance of two tangents to the contour of the particle in a well-defined orientation. Internally, the Feret diameters for as many angles (0°…180°) as possible are calculated and the mean value of the Feret diameters for all orientations is then

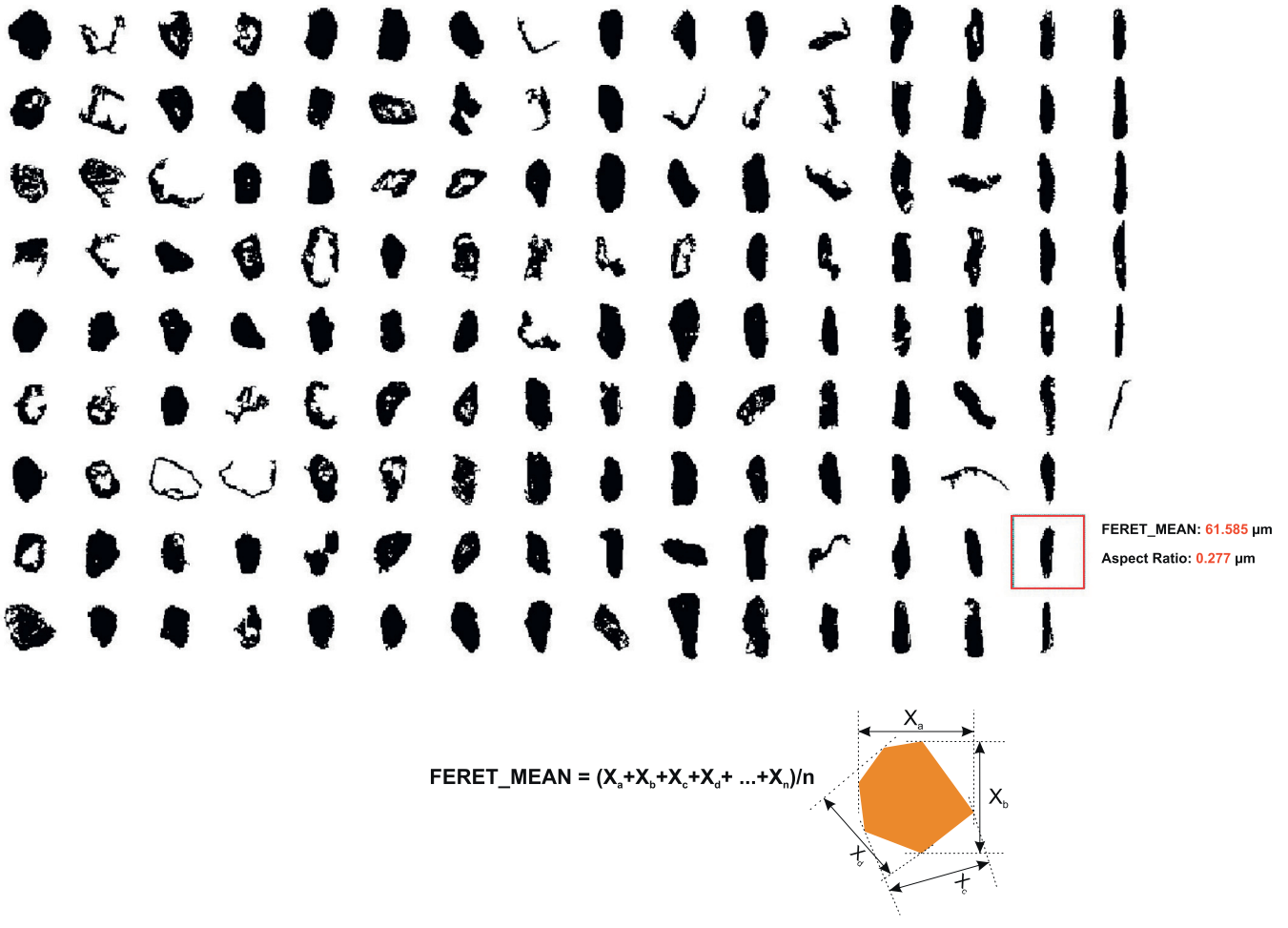

Fig. 3. An illustration of a 2D image of particles and measurement of the Feret diameter and calculation of Feret mean by Qicpic DIA.

used (Fig. 3). Replicate analyses of a series of glass bead and loess samples indicate that the analytical uncertainty, expressed as the coefficient of variation for the median Feret_mean diameter, is in the range 0.5–2.4% (see Table S3).

With respect to grain shape, standard shape descriptors obtained using the Qicpic sensor include the sphericity and the aspect ratio. The sphericity of a particle is defined as the ratio of the EQPC to the actual perimeter of the particle. However, as the EQPC parameters of (partly) transparent particles cannot be accurately measured, the sphericity results are not reported here. Instead, we focus in this study on the aspect ratio, which is defined as the ratio of the minimal to the maximal Feret diameter. The aspect ratio ranges from 0 to 1, corresponding to a range in shape from extremely flat or elongated particles, to perfectly symmetrical particles.

In addition, the software associated with the Qicpic sensor was used to calculate the number of imaged particles for specific size fractions, expressed as parts *per* million (ppm) of the total number of particles analyzed (bulk sample), and in the fraction >16 μm. As our focus was on the silt and (very fine to medium) sand fraction, we reported the particle counts of the >32 μm, >63 μm, >125 μm and >250 μm fractions for detailed analysis.

3. Results

3.1. LD grain size records and endmember modeling of the Quaternary loess sections

The median grain size records, and the proportional contribution of the three endmembers *versus* depth, for the four loess sections, as based on the Fritsch A22 LD measurements, are presented in Fig. 2. The grain size distributions of all the loess and palaeosol samples are expressed as a mixture of the following three endmembers: the very fine sandy endmember EM1, with a modal size of 63 μm; the silty endmember EM2, with a modal size of 37 μm; and the clayey endmember EM3, with a modal size of 22 μm. This demonstrates that within each loess-palaeosol sequence, the variations in the median grain size and proportional contributions of the endmembers relatively clearly define the major lithological loess and palaeosol units. Loess units L1-1, L1-3, L2-1 and L2-3 show high median grain size values and a high proportion of the fine sandy and silty loess endmembers EM1 and EM2. In contrast, the weakly developed palaeosol units L1-2 and L2-2, and especially the well-developed palaeosols S1 and S2, are characterized by low median grain size values and high contributions from the clayey endmember EM3.

The thickness of the glacial loess units displays a downwind decreasing trend: for instance, the thickness of the L1 unit decreases from ~19 m in the HX section, to ~12.5 m in the XF section, ~9 m in the XY section and ~5 m in the DJP section. In contrast, the last interglacial palaeosol unit S1 does not show a clear spatial trend in thickness, being ~2.5 m thick in each loess section (HX, XF and XY).

The endmember contributions also reveal a spatial trend in the four loess sections. The HX loess-palaeosol sequence is characterized by high proportions of the coarse endmembers EM1 and EM2, whereas the XF and XY sequences from the central and southern CLP are dominated by mixture of endmembers EM2 (silty loess) and EM3 (clayey loess). The southernmost DJP loess site is dominated by EM3, with a small additional contribution from EM2, in the L1-1 loess unit.

3.2. Comparison between the LD- and DIA-determined grain size distributions of Quaternary loess

Fig. 4 and Supplementary Fig. S3 present a comparison of the median grain size values obtained using the Qicpic, Helos and Fritsch devices for the four loess sections. The scatter plot in Fig. 4a highlights the strong correlation between the grain size data obtained using the two LD devices, the Fritsch Analysette 22 and the Sympatec HELOS KR. The linear regression ($y = 0.78x + 1.16$, $r^2 = 0.98$) between the two datasets indicates that they are highly consistent, although the Fritsch device tends to produce much lower median grain sizes compared to the Helos device (slope a = 0.78).

Comparisons between the data produced by the Qicpic device *versus* the Fritsch device (Fig. 4b), and the Qicpic device *versus* the Helos device (Fig. 4c) also show strong linear correlations between the datasets, *i.e.* $y = 1.01x - 16.04$ ($r^2 = 0.97$) for the Qicpic-Fritsch comparison, and $y = 1.30x - 22.16$ ($r^2 = 0.99$) for the Qicpic-Helos comparison. These two regression equations display high (negative) intercepts (b), indicating that the Qicpic device tends to systematically 'overestimate' the median grain size by 16–22 μm compared to the two LD devices.

We also compared the grain size distributions of individual loess and palaeosol samples from the four loess sections obtained using the Qicpic device and the two LD devices (Fig. 5). This revealed that the Qicpic device provides a similar grain size mode to the Helos and Fritsch devices for all the loess and (most of the) palaeosol samples. For the L1 loess samples, the Qicpic, Helos and Fritsch devices all show a clear mode at 63 μm for the HX section, 44 μm for the XF section, 37 μm for the XY section and 31 μm for the DJP section. For the S1 and S0 palaeosol samples, the grain size mode measured by the Qicpic device is also closely comparable to the mode obtained using the two LD devices, although the Qicpic mode is slightly coarser than that given by the Helos, and especially the Fritsch device. From the displayed loess and palaeosol grain size distributions, it is also notable that the Qicpic device clearly underestimates the number of particles in the fine tail of the grain size distributions compared to the two highly comparable LD distributions. This

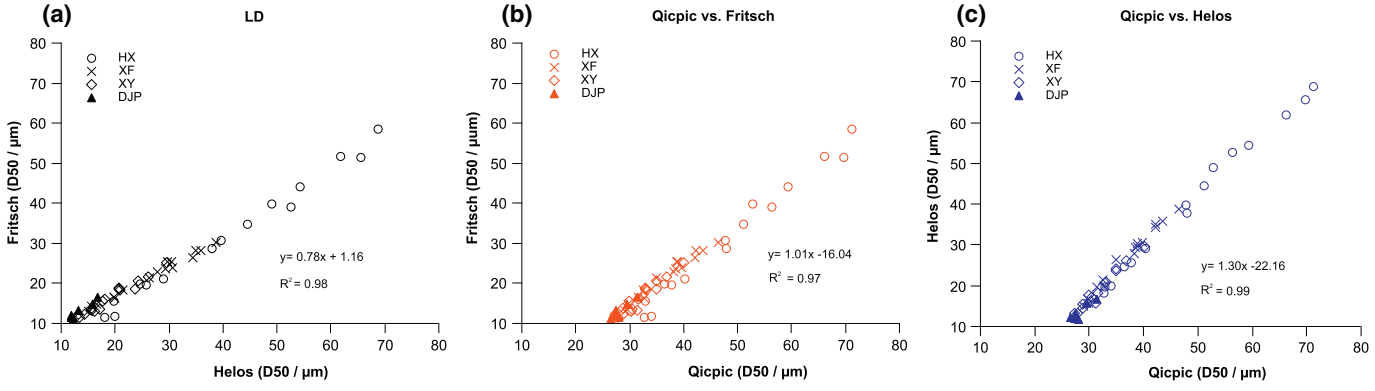

Fig. 4. Comparison of median grain size (D50) measurements made by Qicpic DIA and LD devices (Fritsch and Helos) for samples from the HX, XF, XY and DJP loess sections. (a) Comparison of D50 measured by two LD devices (Fritsch and Helos); (b) comparison of D50 measured by Qicpic DIA and Fritsch LD devices; (c) comparison of D50 measured by Qicpic DIA and Helos LD devices. The median grain size from each instrument was calculated using the GRADISTAT program developed by Blott and Pye (2001).

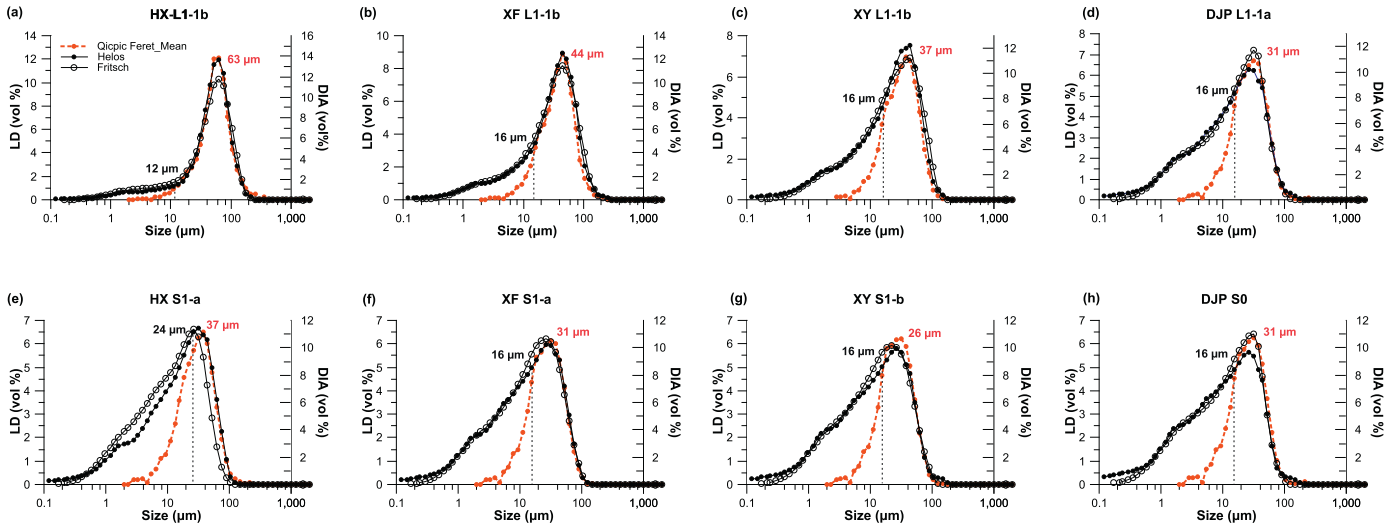

Fig. 5. Grain size distributions of individual samples from loess (L1-1) and palaeosol (S1 and S0 (DJP)) units from the studied loess sections generated by the Qicpic, Helos and Fritsch devices. The sample ID indicated in the figure refers to the notation used in Fig. 2. The numbers in red in the Figure indicate the mode of the grain size distribution for each sample. The dashed lines and the numbers in black in the Figure indicate the deviation boundary between the DIA and LD grain size results.

deviation sets in at, and below, ~12 μm in the case of the coarse-grained loess sample 'HX L1-1b' (Fig. 5a), or ~24 μm in the case of, for instance, the fine-grained palaeosol samples in the HX section ('HX S1-a', Fig. 5e). In general, however, the devices show very comparable results above ~16 μm (Fig. 5b–d and f–h), including the main mode and the coarse tail of the grain size distributions.

3.3. Spatiotemporal variations in the grain size distributions of Quaternary loess as revealed by DIA

The numbers of particles of sizes >32 μm, >63 μm, >125 μm and >250 μm for samples from each of the four loess sections are visualized in Fig. 6, which highlights in great detail the most significant spatiotemporal trends in loess-palaeosol composition.

First, the data demonstrate that the different loess and palaeosol units can be clearly characterized by the contributions (expressed in ppm) of the above size fractions. For example, for the last glacial loess units L1-1 and L1-3, and the penultimate glacial period loess units L2-1 and L2-3, in the HX section, the number of particles of size >32 μm ranges from 19×10^3 to 28×10^3 ppm (Fig. 6a, b). By contrast, the numbers of these particles are significantly lower (9.9×10^3 to 11.9×10^3 ppm) in the poorly-developed palaeosol (PDS) units L1-2 and L2-2 (Fig. 6a and e), but are especially low (6.6×10^3 to 7.2×10^3 ppm) in the well-developed palaeosol units (WDS) S1 and S2 (Fig. 6i). Similar stratigraphic trends in sedimentary composition can be seen in the >32 μm data of the other three loess-palaeosol sequences (XF, XY and DJP) (Fig. 6a, e). These trends are also reflected in the particle counts for the HX section in the >63 μm and >125 μm fractions; clear temporal trends in the >250 μm fraction are, however, lacking for the reasons given below. In the fully glacial L1-1, L1-3, L2-1 and L2-3 loess units of the HX section, the number of particles of size >63 μm ranges from 1.6×10^3 to 2.7×10^3 ppm (Fig. 6b, f), whereas in the >125 μm size fraction, the number of particles ranges from 19 to 76 ppm (Fig. 6c, g), and from 0 to 2 ppm in the >250 μm size fraction. In the PDS sample, between the interstadial units L1-2 and L2-2, the number of particles in the >63 μm, >125 μm and >250 μm size fractions ranges from 339 to 535 ppm (Fig. 6b, f), 3.8 to 6.3 ppm (Fig. 6c, g) and 0.08 to 0.63 ppm (Fig. 6d, h), respectively. In the WDS samples from the interglacial units S1 and S2, the number of particles in the > 63 μm, >125 μm and >250 μm size fractions ranges from 185.6 to 240.2 ppm (Fig. 6j), 1.5 to 1.8 ppm (Fig. 6k), and 0 to 0.06 ppm (Fig. 6l), respectively. For the XF and XY sections, and to a lesser extent also for the DJP section, it can be observed that the loess, PDS and WDS units are also clearly distinguishable by their particle counts in the >63 μm and >125 μm fractions. This is highlighted in Fig. 6m–p, in which the average number of particles in different size classes is summarized for all four sections. These figures clearly show a decrease in the 'coarse' particle numbers from the glacial loess units to the interstadial PDS units, and to the interglacial WDS unit, in the HX, XF and XY sections, and, to a lesser extent, in the DJP section.

A second key observation is that the Qicpic data (Fig. 6a–l) show a notable southward decrease in the number of silt and fine sand particles found in the loess and palaeosol units; this is highlighted in Fig. 6m–p, in which the average compositions of the loess, PDS and WDS units (Fig. 2) are presented. For example, the average number of particles >32 μm in the glacial loess samples ('L' in Fig. 6m) is 22.5×10^3 ppm in the HX section on the northern CLP, but decreases to 12.9×10^3 ppm in the XF section, 9.1×10^3 ppm in the XY section and 5.2×10^3 ppm in the southernmost DJP section. Similar spatial trends in the composition of the loess units along the HX-DJP transect are reflected in the particle counts in the >63 μm (Fig. 6n) and >125 μm fractions (Fig. 6o), which range between 2.6×10^3 to 91 ppm and 41.5 to 0.5 ppm, respectively. The average particle count in the >250 μm fraction also shows an apparent spatial trend in the loess (L) units (Fig. 6p), but considering the large spread in the data (see Fig. 6d and h), and the very low particle counts (<1 ppm), this 'trend' is considered insignificant.

The average PDS compositions, and, to a lesser degree, the WDS compositions, display the same spatial trends in the >32 μm, >63 μm, and even the >125 μm fractions, although these trends are not as striking as in the glacial loess units. The spatial trends in the average PDS compositions are not described in detail here; they are intermediate between the loess and the WDS compositions. The average number of particles of size >32 μm in the WDS units is ~6.9×10^3 ppm in the HX section, 5.6×10^3 ppm in the XF section, and 4.8×10^3 ppm in the XY section (Fig. 6m). The average number of particles of size >63 μm in the WDS units decreases from 213 ppm in the HX section, to 123 ppm in the XF section, and 86.7 ppm in the XY section (Fig. 6n). The two coarsest fractions do not show any (clear) spatial trends: <1 ppm of particles of size >125 μm is found in the WDS units, except in the HX section, in which their concentration reaches a meager 1.6 ppm; the number of particles >250 μm is well below 0.2 ppm in the WDS units.

As shown above (Section 3.2, Fig. 5), the grain size distributions measured using Qicpic DIA deviate from the grain size distributions measured by LD devices when the particle size is <16 μm. Thus, in

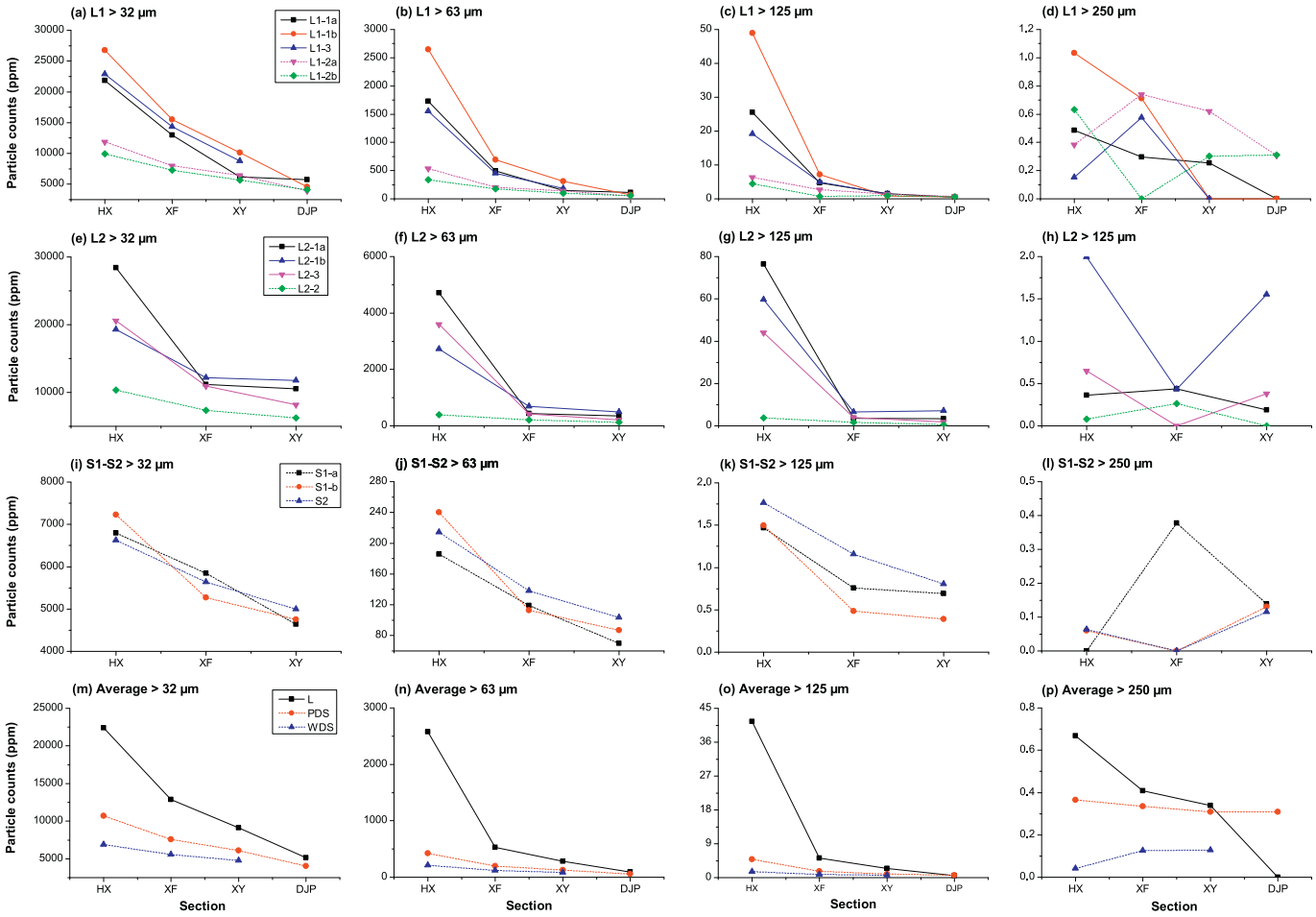

Fig. 6. Particle counts in the coarse silty (>32 μm) and very fine to medium sandy fractions (>63 μm, >125 μm and >250 μm) expressed in parts *per* million (ppm) with respect to total particle count in the bulk samples extracted from the loess (L1, L2) and palaeosol (S1, S2) units of the four loess sections (HX, XF, XY and DJP). Sample ID's (in panels a–l) refer to the notation used in Fig. 2. Abbreviations used in panels m–b: L = loess; PDS = poorly-developed palaeosol; WDS = well-developed palaeosol.

order to eliminate the effect of the number of fine particles, and to focus on the coarse tail of the grain size distributions analyzed correctly by both the DIA and LD devices, we recalculated the content of each fraction (using particle sizes of >32 μm, >63 μm, >125 μm and >250 μm) based on the numbers of particles >16 μm (Supplementary Fig. S4). The recalculation increased the number (×10) of counted coarser particles in the bulk sediments, thus highlighting the compositional trends in the coarse tails of each of the grain size distributions in more detail. Nevertheless, the spatiotemporal patterns are very similar to those indicated in Fig. 6, and will therefore not be explained in detail here.

3.4. Particle shape distributions within Quaternary loess as revealed by DIA

First, we investigated the grain shape distribution (aspect ratio) of each loess sample from the four loess sections (Supplementary Fig. S5). Unlike the grain size distributions observed in loess samples, no obvious temporal variations are discernible in loessic grain shape distributions (Supplementary Fig. S5). Although large variations have been observed in the coarse ends (>80 μm) of the shape distribution spectra (Supplementary Fig. S5), the differences are probably due to the limited number of measured grains (Fig. 6), meaning that the pattern is of less statistical significance. We then focused on the 16–63 μm size fraction, for which abundant particles were measured (Fig. 6 and Supplementary Fig. S4) in an attempt to illustrate the average shape distribution of samples from loess, PDS and WDS units for the HX, XF, XY and DJP loess sections (Fig. 7a–d). It can be seen that for all samples in the loess, PDS and WDS units, for particles in the 16–63 μm size range, the aspect ratio of the particles varies from 0.55 to 0.71, and decreases as a function of increasing grain size (Fig. 7a–d). For most of the samples, the differences in the grain shape distributions of each unit fall within the error bars (standard deviation of the mean; Fig. 7a–d), except for the loess unit in the HX section, which displays relatively larger deviations in the 50–63 μm size range (Fig. 7a). In addition, the HX section on the northern CLP reveals that for particles in the 16–35 μm size range, the average aspect ratios of the particles are almost identical in the loess, PDS and WDS units. In contrast, for particles in the 35–63 μm size range, the aspect ratio of particles in the loess units is slightly higher than in the PDS and WDS units (Fig. 7a), indicating that more symmetrical coarse silt grains are present in the silty loess layers than in the palaeosol units. The XF section on the central CLP does not reveal any specific variation in the aspect ratio between loess and palaeosol units. The XY section on the southern CLP in turn demonstrates that in the 16–63 μm size range, the aspect ratio of particles in the WDS units is higher than that of particles in the loess and PDS units (Fig. 7c). For the DJP section, which only reaches L1, the aspect ratio of particles in the PDS units is slightly higher than in the loess units in the 16–55 μm size range.

Fig. 7e–g compares the grain shape distributions for the different units of the four loess-palaeosol sequences. In the loess units (Fig. 7e), the aspect ratio for particles in the 35–63 μm size range decreases from the HX to the XF section, and subsequently to the XY and then the DJP section, while for particles <30 μm, the aspect ratio value of the HX section is relatively lower than at the three southern sites. By contrast, in the WDS units (Fig. 7g), particles in the 20–50 μm size

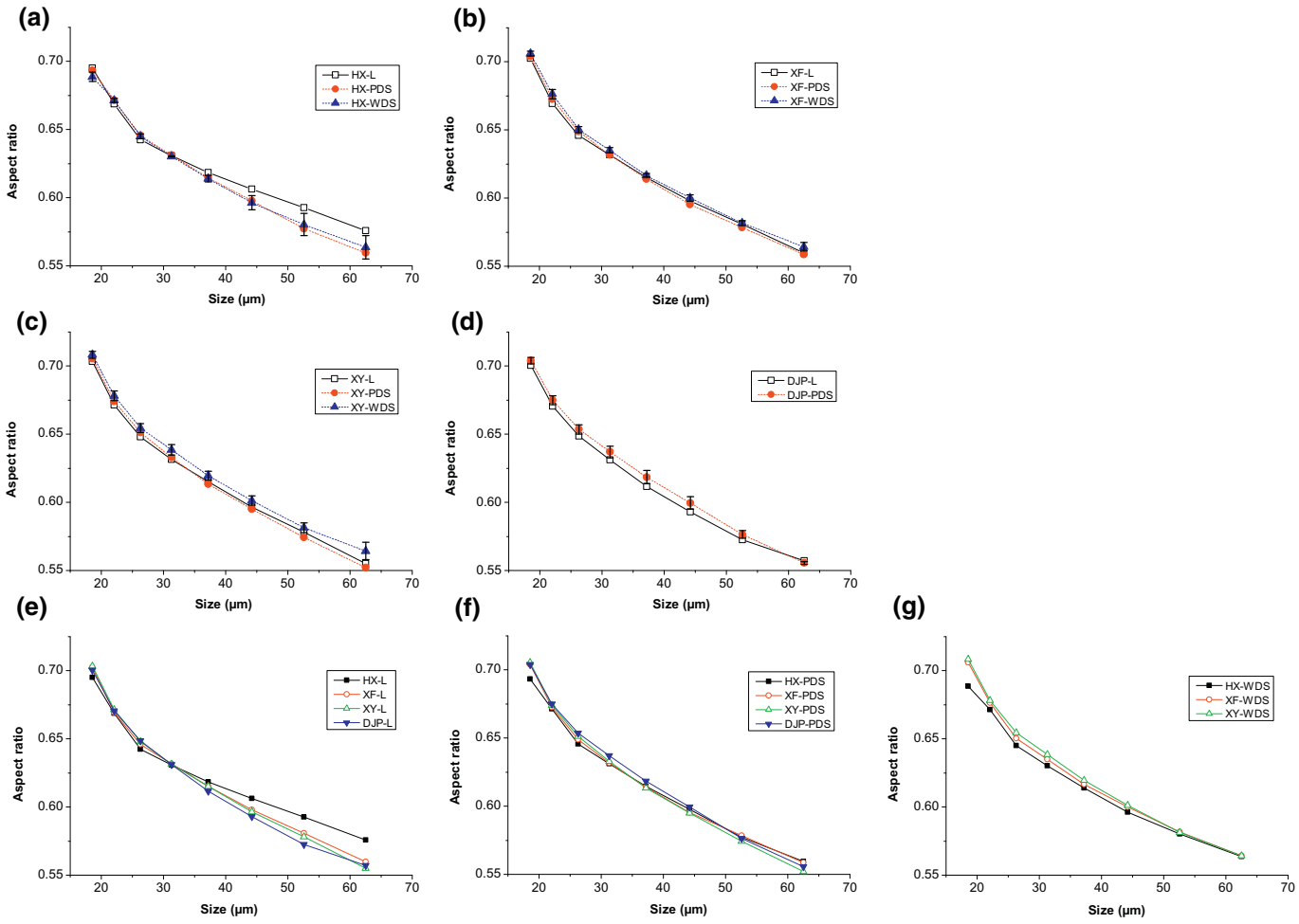

Fig. 7. Average grain shape distribution spectra with error bars for samples from the loess (L), poorly-developed palaeosols (PDS) and well developed palaeosols units (WDS) analyzed from the four loess sections: (a) HX; (b) XF; (c) XY; and (d) DJP. Panels (e)–(g) show the spatial comparison of the grain shape distribution spectra of different units from the four loess sections: (e) loess units; (f) poorly-developed palaeosols; and (g) well-developed palaeosols.

range at the southern XY site show relatively higher aspect ratios than at the northern XF and HX sites. No obvious spatial variation in particle aspect ratios was observed in the PDS units for the four loess sequences (Fig. 7f).

3.5. Particle size and shape distributions in Late Miocene-Pliocene Red Clays as revealed by DIA

Fig. 8a–c display the number of particles of sizes >32 μm, >63 μm and >125 μm in the four Red Clay sequences in comparison with those found in the loess and palaeosol samples. As mentioned in Section 3.2, the accuracy of the Qicpic DIA for loess sediments is likely limited to particles >16 μm. Thus, we here focus on the coarse fraction in the Red Clay deposits and the numbers of particles of each fraction calculated, based on counts of particles of sizes >16 μm, instead of the numbers of particles within the whole bulk sample (Supplementary Fig. S6). No major temporal variations were observed in the number of particles in the >32 μm and >63 μm size fractions throughout individual Red Clay sequences (Fig. 8a, b), while for particles of size >125 μm, the counts demonstrate relatively larger variations in the Red Clays of the JL and LT Fms, compared to the BD Fm and DW (Fig. 8c). The average number of particles of size >32 μm is 11×10^4 ppm in the BD Fm, 8.6×10^4 ppm in the JL Fm, 6.3×10^4 ppm in the DW Red Clay, and 7.0×10^4 ppm in the LT Fm Red Clays. For particles >63 μm, the average number is 5.2×10^3 ppm in the BD Fm, 3.8×10^3 ppm in the JL Fm, 686.6 ppm in the DW Red Clay, and 2.0×10^3 ppm in the LT Fm Red Clays. In general, Red Clay is a more fine-grained sediment than Quaternary loess (Supplementary Fig. S7), and smaller numbers of coarse silt (32–63 μm) and very fine sand (63–125 μm) particles were therefore observed in the Red Clay samples than in the loess samples; indeed, the Red Clay particle component is more comparable to the PDS and WDS palaeosol units in the loess sequence. Spatially, it is clear that the BD and JL Fm Red Clay on the northeastern CLP contain more coarse silt (32–63 μm) and very fine sand particles (63–125 μm) than the Red Clays in the DW and LT Fm in the sections we studied on the western and southern CLP (Fig. 8a, b). However, a notable number of 'giant' particles (>125 μm) has also been observed in both the JL Fm Red Clay of the northern CLP, and the LT Fm Red Clay of the southern CLP. This number is comparable to that observed in the XF loess units.

Supplementary Fig. S8 shows the grain shape distributions of samples from the four Red Clay sections. In general, no obvious temporal variation was observed in the aspect ratio distributions of particles in the 16–60 μm size range in the BD, JL, DW, and the upper part of the LT Fm Red Clays (Supplementary Fig. S8). Thus, only the averaged grain shape distribution for each section is presented here (Fig. 9a). In the 16–63 μm size range, the particle aspect ratios vary from 0.70 to 0.58 in the BD Fm, 0.71 to 0.59 in the JL Fm, 0.71 to 0.56 in the DW Red Clay, and 0.72 to 0.55 in the LT Fm Red Clays. Notably, Red Clay sample LT-1, at the bottom of the LT Fm, is prominent because of its distinctive grain shape distribution spectra compared to the other samples

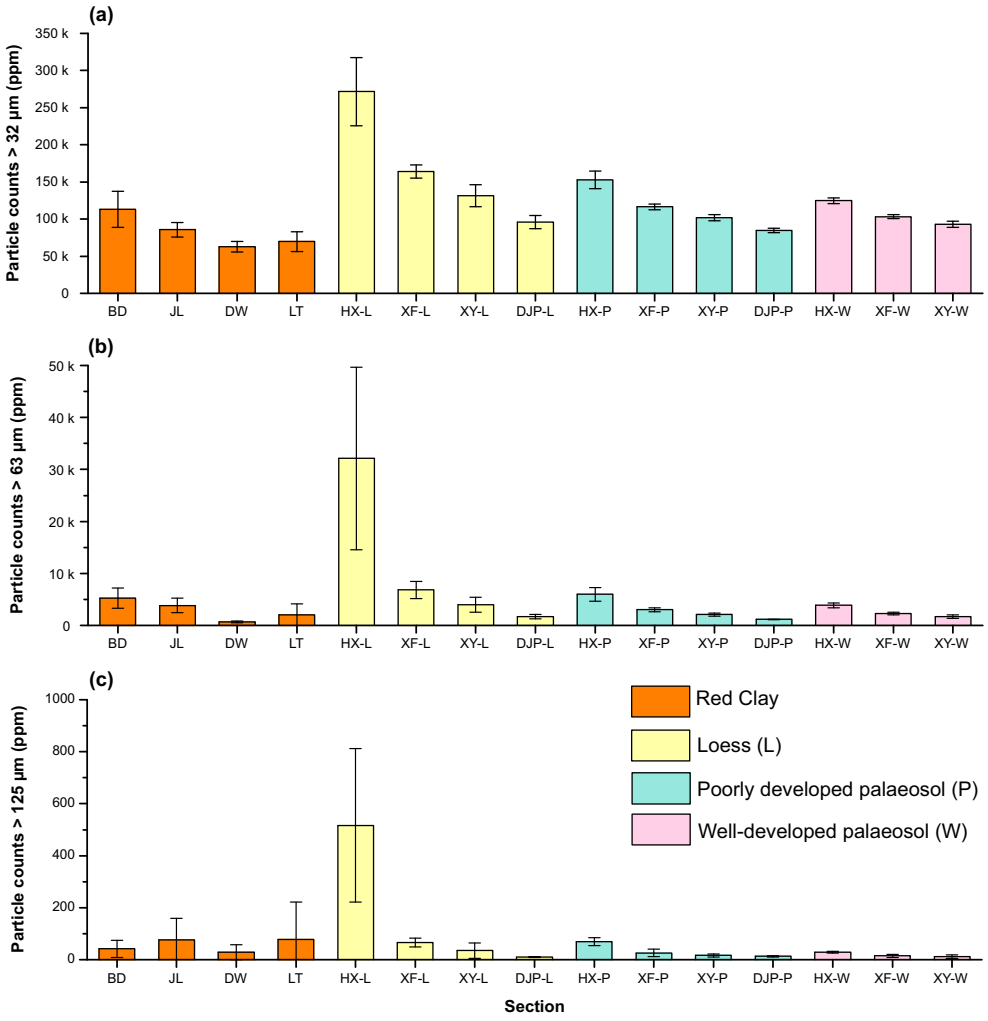

Fig. 8. Average numbers, with error bars, for particles of size fractions: (a) >32 μm; (b) >63 μm; and (c) >125 μm observed in Red Clay samples from the BD, JL, DW and LT compared to the quantities of these fractions seen in the loess (L), poorly-developed palaeosols (PDS) and well-developed palaeosols (WDS) of the Quaternary loess-palaeosol sequences (HX, XF, XY and DJP). Note that the calculations are based on the numbers of particles of size >16 μm instead of the total particle counts from the bulk samples.

(Fig. 9a and Supplementary Fig. S8). Particles in the 16–55 μm size range in the LT-1 sample display a noticeably lower aspect ratio than in the overlying samples.

In Fig. 9b–d, we compare the averaged grain shape distribution of Red Clay with that of loess, PDS and WDS units. In the Red Clay samples, the particle aspect ratios are observed to decrease with an increase in grain size, similar to what is seen in the Quaternary loess and palaeosol samples (Fig. 9). In general, in the 16–60 μm size range, the aspect ratio of particles in the LT and JL Fms is notably higher than in the loess (except for HX-L), PDS and WDS units. The grain shape distribution of particles in the BD Fm is comparable to those observed in the loess, PDS and WDS units in the 16–40 μm size range, and is relatively higher than those seen in the PDS and WDS units in the 40–63 μm size range. The grain shape distribution of particles in the DW Red Clay largely overlaps with both the loess and palaeosol (PDS and WDS) units in the 16–63 μm size range (Fig. 9b–d).

4. Discussion

4.1. Performance of DIA in measuring silt-sized sediments

Comparison of the DIA grain size distribution with the results of LD analysis indicates that DIA provides a similar grain size distribution and grain size mode to the LD devices for particles >16 μm (Fig. 5). The median grain size (D50) dataset obtained from DIA is also highly positively correlated with that of the LD devices, suggesting that DIA is capable of capturing the main particle characteristics (Fig. 4). In addition, unlike the LD grain size analysis, which only provides the volume percentage for the different fractions in the bulk sediments, DIA is able to count the numbers of particles measured in various size fractions; the proportional contribution of grains in a certain size fraction can thus be expressed in parts *per* million (ppm). Both the analyses based on bulk sediment (Fig. 6), and upon the coarse fraction of the sediment (Supplementary Fig. S4), reveal the same spatiotemporal pattern in loess-palaeosol sequences, and are highly comparable with the D50 and endmember modeling results based on LD grain size analysis (volume percentage) (Fig. 2). This further indicates that the silty and sandy fractions (>16 μm), measured by Qicpic DIA, are precisely and reliably documented, and that any disparities between the Qicpic and LD grain size distributions (Figs. 4 and 5) represent a systematic offset.

It is notable that DIA tends to underestimate the clay fraction in bulk sediments, and, as a consequence, the grain size spectra are more skewed towards coarser particles than in LD results (Figs. 4 and 5). This is probably because the pixel size of the Qicpic camera currently used is 2 × 2 μm, and small particles are consequently (partly) out of focus and fail to be imaged by the camera. Thus, in this study, the size limitation for the precise analysis of particles is set at 16 μm. Tysmans et al. (2006) applied DIA using different equipment (RapidVue,

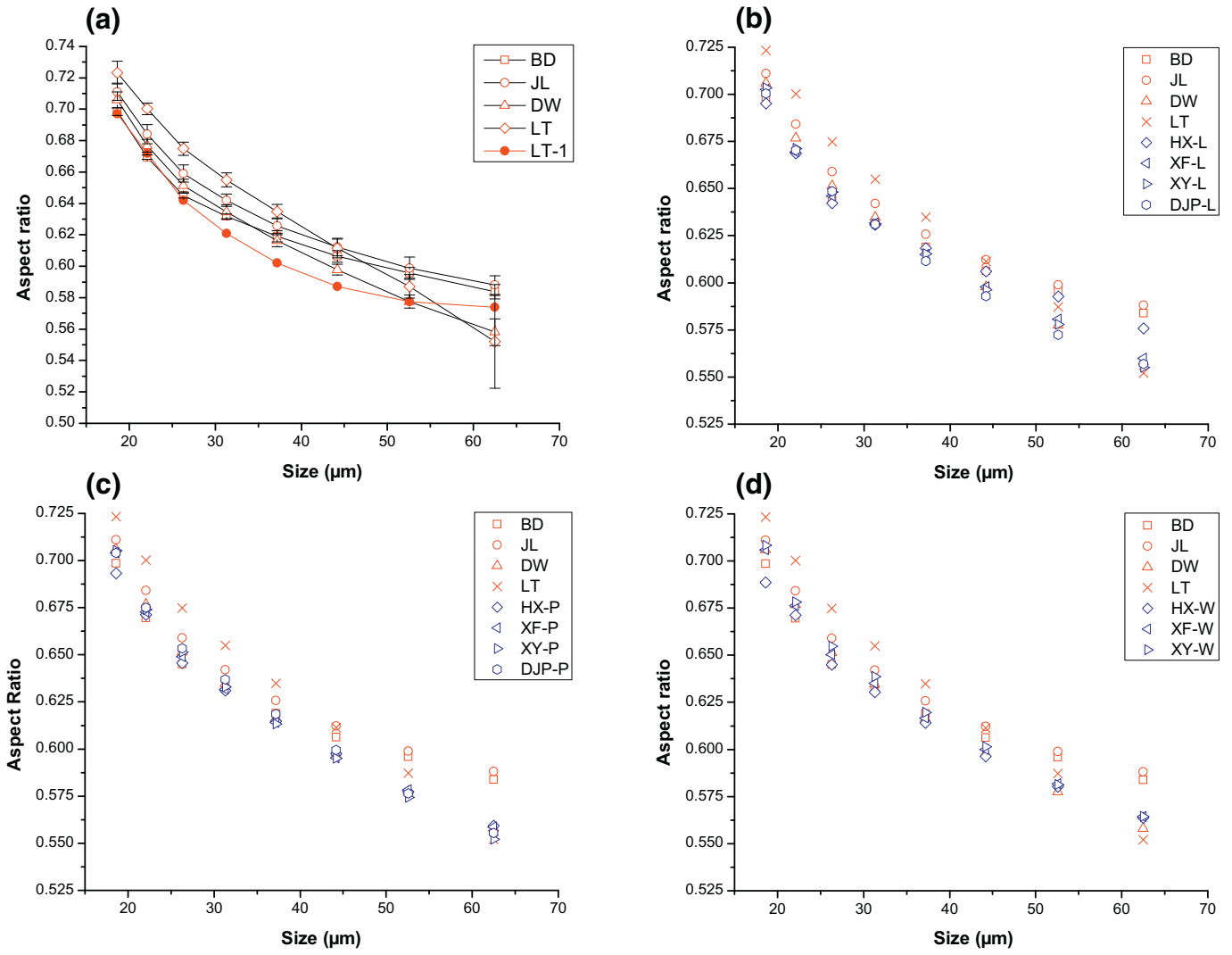

Fig. 9. Average grain shape distribution for silt-sized particles (16–63 μm) in the samples taken from Red Clay sections (a, with error bar), compared with loess (b) and palaeosol samples (c and d).

Beckman Coulter Company) to examine silty loess from Belgium. These authors similarly indicated that DIA measurements are more accurate for larger particles with a finer resolution, and consequently the lower particle size limit of their study's analyses was set at 20 μm. Nevertheless, the accuracy of DIA in measuring finer particles could be improved in the future by increasing the camera's resolution.

It was also observed during the course of this study that transparent particles may not have been fully imaged by the Qicpic camera, which have resulted in the image representing a smaller projection area than the actual one. Thus, the sphericity calculated according to the projection area of the particles tends to be underestimated (Supplementary Table S2 and Supplementary Fig. S2). In this case, sphericity should be carefully used when defining variations in particle shape. The aspect ratio appears to be more reliable in describing the actual shape characteristics of particles in the current setting.

4.2. Transport pathways as revealed by DIA grain size records in the Quaternary loess-palaeosol sequences

Endmember modeling of the grain size distributions of loess samples reveals a clear spatiotemporal pattern along the four loess-palaeosol sequences during the last two glacial and interglacial periods (Fig. 2). The loess units are mainly composed of coarse EM1 and EM2, while the palaeosol units are characterized by a high proportion of fine EM3. Spatially, the sandy EM1 and silty EM2 decrease from the northern HX section to the southern DJP section, while the clayey EM3 increases from the northern section to the southern sections. DIA also successfully differentiates loess units from poorly- and well-developed palaeosol units, as indicated by the numbers of coarse grains in the sediments (Fig. 6). Loess samples are characterized by high numbers of coarse silty (>32 μm) and sandy (>63 μm and 125 μm) particles, whereas palaeosol samples contain relatively smaller numbers of coarse grains.

Previous studies have indicated that loess on the CLP is transported from the adjacent arid desert areas by northerly and northwesterly monsoonal winds (Liu and Ding, 1998; Lu and Sun, 2000; Nugteren and Vandenberghe, 2004; An et al., 2014) and/or is first carried by the Yellow River to the Yinchuan-Hetao Graben (the Yellow River floodplain), and from there transported by winter monsoonal winds to the Mu Us Desert, and eventually to the CLP (Stevens et al., 2013; Nie et al., 2015). During aeolian transport, the heavy, coarse particles first descend in the proximal area near the source region (*i.e.* the northern CLP), while the light and fine material is released later over intermediate and distant areas (*i.e.* the central and southern CLP). Thus, a sedimentation gradient is apparent on the CLP from north to the south (Ding et al., 2002; Kohfeld, 2003; Nugteren and Vandenberghe, 2004; Prins et al., 2007). The Qicpic DIA also clearly characterizes such a gradient in the grain size records of the loess-palaeosol sequences on the CLP during the last two glacial and interglacial periods which is consistent

with the endmember modeling of the grain size records from LD analyses (Fig. 2). Our DIA of the four loess-palaeosol sequences reveals a decreasing trend in the numbers of particles in the >32 μm, >63 μm and >125 μm size fractions from the northern HX section to the southern DJP section. In addition, the particle numbers in coarse silty and fine sandy fractions (>32 μm, >63 μm and >125 μm) are significantly higher in the loess units than in the palaeosol units, and the gradient is more prominent in the loess units than in the palaeosol units of the four loess sequences (Fig. 6 and Supplementary Fig. S4). This indicates that the spatial variation in grain sizes from the four loess sections is more marked during the glacial (L1 and L2) than the interglacial periods (S1 and S2) (see Fig. 6m, n, o). Prins and Vriend (2007) also observed a marked north-to-south decrease in the flux rate (EM1 and EM2) in the loess units L1-1, and a less steep spatial trend in the palaeosol unit S1. These results all indicate the occurrence of strong storm events and/or strengthened N-NW monsoonal winds during glacial periods, and a weaker dust supply pattern during interglacials.

Pye (1994) suggested that it is possible to use the rate of change in grain size, roundness and sphericity to make inferences about temporal changes in the provenance of dust material and the dust-transporting winds that blow across the CLP. It is still under debate whether temporal shifts exist in the provenance of Quaternary dust. Based on single-grain zircon U-Pb age dating, Xiao et al. (2012) suggested a varying aeolian provenance for the sediments of the CLP over glacial-interglacial cycles. Bird et al. (2015) also indicated that the provenance of loess and palaeosol units varies through time, but that the shifts are not consistent with changes between glacial and interglacial periods, and *vice versa*. However, Che and Li (2013) inferred that no spatiotemporal heterogeneities of zircon ages have in fact been observed for the dust deposits on the CLP. A recent study based on a large dataset of detrital zircon U-Pb ages (Licht et al., 2016) demonstrated that the sources of glacial loess and interglacial palaeosols cannot be easily differentiated, since the source signature for the interglacial palaeosols is significantly dampened by the recycling of older loess. No distinctive temporal trends are seen in the grain shapes of loess and palaeosol samples during the Quaternary from our DIA results, either. Therefore, our results likely indicate that particles in the loess and palaeosol units have at least been subjected to an analogical shape-sorting process during their transportation.

4.3. Aeolian origin of the Red Clay deposits as indicated by grain size and shape inferred from DIA

DIA reveals that the numbers of silty (>32 μm) and very fine sandy (>63 μm) particles in the four Red Clay sequences are comparable to those in the loess units of the southern CLP loess section (DJP), and in the palaeosol units of the Quaternary loess-palaeosol sequences (Fig. 8). This indicates that the composition of the coarse silty particles in Red Clay deposits is very similar to that of the loess found on the southern CLP, as well as to interglacial palaeosols. Previous studies based on LD grain size results have demonstrated that the mean/median grain size and the coarse fraction content in the bulk Red Clay samples systematically decrease southward across the CLP (Miao et al., 2004; Yang and Ding, 2004; Wen et al., 2005). Endmember modeling of the grain size distribution of three Red Clay sections (Shang et al., 2016) has also demonstrated that the BD Fm and JL Fm Red Clays on the northeastern CLP are silt-dominated, while the DW on the western, and the LT Fm Red Clays on the southern CLP are clay-rich (Supplementary Fig. S1). Our DIA on the same Red Clay sections has also demonstrated such spatial variations. The silty (>32 μm) and very fine sandy (>63 μm) particles are more abundant in the BD and JL Fm on the northeastern CLP than in the LT Fm and DW Red Clays (Fig. 8). Both the content of coarse silty particles in the Red Clay samples, and its southward decrease across the CLP, suggest that coarse silty particles in the late Miocene-Pliocene Red Clays are mainly windblown products and may have been subjected to transportation processes similar to those experienced by the Quaternary loess. The numbers of sandy fractions of size >125 μm and >250 μm in the bulk samples of Red Clays in general are <10 ppm (Supplementary Fig. S6) and <1 ppm, respectively, and are therefore not discussed in detail here.

In general, the shape distribution of particles in Red Clay samples displays a similar pattern to that seen in Quaternary loess and palaeosol samples, showing a decrease in the aspect ratio with an increase in grain size. In particular, the grain shape distributions in the DW Red Clay largely overlap with the spectra of the loess and palaeosol units. This is consistent with the field observation that the DW Red Clay on the western CLP is uniform loessic Red Clay (Hao and Guo, 2004). The grain shape distribution of particles in the BD Fm is also comparable to that in the loess, PDS and WDS units in the 16–40 μm size range, indicating a similar transportation process for these particles found in the BD Red Clay, as compared to the Quaternary loess. The aspect ratio of particles in the JL and LT Fm Red Clays (excluding sample LT-1) is slightly higher than in the comparable loess and palaeosol units. This may be partly attributable to strong chemical weathering processes during soil formation that have altered the particles towards more symmetrically-shaped silt particles in these two sections (Kaakinen and Lunkka, 2003; Zhu et al., 2008; Shang et al., 2016). The lowermost sample (LT-1) from the fluvial-influenced basal part of the LT Fm (Supplementary Fig. S1) displays a size-aspect ratio spectrum distinctive from the upper aeolian LT Fm Red Clay samples (Fig. 9a). This probably suggests that DIA of particle shape is capable of distinguishing aeolian from non-aeolian contributions in bulk sediments.

4.4. Shape sorting during the wind transportation of silty particles

The exact nature of shape sorting during the transportation of aeolian sediments, particularly of silty particles, remains unclear. Mazzullo et al. (1992) stated that aeolian transportation is very selective regarding grain size and shape. Their results indicated that there is a downwind increase in the roundness of quartz silty grains due to preferential transport, or the shape sorting, of more rounded grains. They explained that during aeolian entrainment, rounded (spherical) grains are lifted to a greater height above the surface than more angular grains, and can thus experience the greatest forward acceleration, traveling more rapidly, and thus being transported to more distant areas, than less rounded grains. However, Pye (1994) pointed out that because of the relatively low mass of silt-size quartz grains, relatively little energy is released when they collide during suspended transport, and, as a consequence, the rounding of the edges of silty grains by chipping and abrasion during inter-grain collisions is not significant. He further indicated that flatness, rather than roundness, is actually the principal shape factor that influences differential settling rates, and that a flattened grain will be transported further downwind than a spherical one because of the lower settling velocity of the former. Our results appear to lend more support to the latter view. Based on the statistics for 0.8–20 million particles *per* sample (Table S1), in the 35–63 μm size range, the aspect ratio of coarse silty loess particles decreases from the HX to the XF section, then to the XY section, and finally to the DJP section. Assallay et al. (1998) also suggested that a significant proportion of the quartz silty grains seen in the aeolian loess sediment are platy and blade-shaped due to the high-energy comminution process which occurs during the formation of silt-sized quartz particles. However, our DIA currently provides only 2D images of these particles, and we are therefore not always able to differentiate spherical grains from disc-shaped grains. Our results indicate that in the coarse silt-sized fraction, the larger size grains found at the more distant loess sites (sections XY and DJP) are less symmetrical (low aspect ratio) and/or exhibit greater numbers of flattened grains, at least in the loess units.

Our DIA results demonstrate a systematic pattern whereby the average particle aspect ratio decreases with an increase in grain size, indicating that small particles are on average more symmetrical than large ones. The size-aspect ratio coupling holds for all loess samples despite the site position, meaning that this phenomenon is related to aeolian

transport and sedimentation in general, *i.e.* characteristic for the suspension transport/sorting process itself. We presume that this size-shape pattern has implications for the settling velocity of the particles. The fall velocity is influenced by the aerodynamic properties of particles (surface area, particle shape and density), and their fluid properties, *i.e.* density and viscosity (Újvári et al., 2016). Thus, for two particles with the same density and volume, the one with a larger surface area will have a smaller fall velocity and settles more slowly than that with a smaller surface area. Therefore, a combination of grain size and shape may group particles into distinct 'aerodynamic endmembers' which might provide more quantitative information on the wind strength present during the transportation of these 'dynamic populations' (*cf.* Weltje and Prins, 2003) than the end-member modeling data do which are solely based on LD particle size data. Our future research on aeolian sediments will therefore focus on the end-member modeling of combined particle size-shape data obtained by dynamic image analysis.

5. Conclusions

This study sheds light on using the DIA of particle size and shape to examine the transportation processes experienced by the silty particles found in aeolian sediments. We evaluated the performance of the DIA of grain sizes in samples from four loess-palaeosol sequences found across the CLP in northern China. The results revealed that DIA successfully differentiates loess units from palaeosol units and, in addition, clearly characterizes spatiotemporal variations in the grain size records of these loess-palaeosol sequences for the last two glacial and interglacial periods. The results were consistent with grain size records derived from LD analyses. DIA is also able to characterize spatial variations in the grain sizes of the more fine-grained Red Clay deposits underlying the Quaternary loess, and can probably distinguish any fluvial contributions to Red Clay sequences. DIA of the grain shapes of loess-palaeosol sequences and Red Clay deposits revealed a systematic pattern whereby aspect ratio decreased with increasing grain size, indicating that systematic shape sorting occurred during aeolian transportation of these particles. This study therefore indicates that the DIA of grain size and shape is a potentially useful tool for the reconstruction of the transportation pathways and for fingerprinting the source of silt-sized aeolian sediments.

Acknowledgements

We are grateful to Martine Hagen and Unze van Buuren at the Vrije Universiteit, Amsterdam for their support with grain size analysis. Jef Vandenberghe is thanked for providing loess samples from the Huanxian, Xifeng and Xunyi loess sections. YS should like to thank the Doctoral Program in Geosciences of the University of Helsinki for travel funding. We thank Gert Jan Weltje and Jasper Knight for editorial work and two anonymous reviewers for their helpful and constructive reviews of the manuscript. This work was supported by AK's Academy of Finland funding, projects nos. 257850, 264935 and 292827.

Appendix A. Supplementary data

Supplementary data to this article can be found online at https://doi.org/10.1016/j.sedgeo.2017.12.001.

References

Alonso-Zarza, A.M., Zhao, Z., Song, C.H., Li, J.J., Zhang, J., Martín-Pérez, A., Martín-García, R., Wang, X.X., Zhang, Y., Zhang, M.H., 2009. Mudflat/distal fan and shallow lake sedimentation (upper Vallesian–Turolian) in the Tianshui Basin, Central China: evidence against the late Miocene eolian loess. Sediment. Geol. 222, 42–51.

Altuhafi, F., O'Sullivan, C., Cavarretta, I., 2013. Analysis of an image-based method to quantify the size and shape of sand particles. J. Geotech. Geoenviron. 139, 1290–1307.

An, Z.S., Kutzbach, J.E., Prell, W.L., Porter, S.C., 2001. Evolution of Asian monsoons and phased uplift of the Himalaya-Tibetan plateau since Late Miocene times. Nature 411, 62–66.

An, Z.S., Sun, Y.B., Zhou, W.J., Liu, W.G., Qiang, X.K., Wang, X.L., Xian, F., Cheng, P., Burr, G.S., 2014. Chinese Loess and the East Asian Monsoon. In: An, Z.S. (Ed.), Late Cenozoic Climate Change in Asia: Loess, Monsoon and Monsoon-arid Environment Evolution. Springer, Netherlands, pp. 23–143.

Assallay, A., Rogers, C.D.F., Smalley, I.F., Jefferson, I.F., 1998. Silt: 2–62 μm, 9–4φ. Earth Sci. Rev. 45, 61–88.

Bird, A., Stevens, T., Rittner, M., Vermeesch, P., Carter, A., Andò, S., Garzanti, E., Lu, H., Nie, J., Zeng, L., Zhang, H., Xu, Z., 2015. Quaternary dust source variation across the Chinese loess plateau. Palaeogeogr. Palaeoclimatol. Palaeoecol. 435, 254–264.

Blott, S.J., Pye, K., 2001. GRADISTAT: a grain size distribution and statistics package for the analysis of unconsolidated sediments. Earth Surf. Process. Landf. 26, 1237–1248.

Blott, S.J., Pye, K., 2006. Particle size distribution analysis of sand-sized particles by laser diffraction: an experimental investigation of instrument sensitivity and the effects of particle shape. Sedimentology 53, 671–685.

Blott, S.J., Pye, K., 2008. Particle shape: a review and new methods of characterization and classification. Sedimentology 55, 31–63.

Che, X., Li, G., 2013. Binary sources of loess on the Chinese Loess lateau revealed by U–Pb ages of zircon. Quat. Res. 80, 545–551.

Deplazes, G., Lückge, A., Stuut, J.-B.W., Pätzold, J., Kuhlmann, H., Husson, D., Fant, M., Haug, G.H., 2014. Weakening and strengthening of the Indian monsoon during Heinrich events and Dansgaard-Oeschger oscillations. Paleoceanography 29:99–114. https://doi.org/10.1002/2013PA002509.

Ding, Z.L., Sun, J.M., Liu, T.S., Zhu, R.X., Yang, S.L., Guo, B., 1998. Wind-blown origin of the Pliocene red clay formation in the central Loess Plateau, China. Earth Planet. Sci. Lett. 161, 135–143.

Ding, Z.L., Derbyshire, E., Yang, S.L., Yu, Z.W., Xiong, S.F., Liu, T.S., 2002. Stacked 2.6-Ma grain size record from the Chinese loess based on five sections and correlation with the deep-sea $\delta^{18}O$ record. Paleoceanography 17. https://doi.org/10.1029/2001PA000725.

Eshel, G., Levy, G.J., Mingelgrin, U., Singer, M.J., 2004. Critical evaluation of the use of laser diffraction for particle-size distribution analysis. Soil Sci. Soc. Am. J. 68, 736–743.

Fedotov, G.N., Shein, E.V., Putlyaev, V.I., Arkhangel'skaya, T.A., Eliseev, A.V., Milanovskii, E.Y., 2007. Physicochemical bases of differences between the sedimentometric and laser-diffraction techniques of soil particle-size analysis. Eurasian Soil Sci. 40, 281–288.

Folk, R.L., Ward, W.C., 1957. Brazos River bar: a study in the significance of grain size parameters. J. Sediment. Petrol. 27, 3–26.

Guo, Z.T., Peng, S.Z., Hao, Q.Z., Biscaye, P.E., Liu, T.S., 2001. Origin of the Miocene–Pliocene Red-Earth Formation at Xifeng in Northern China and implications for paleoenvironments. Palaeogeogr. Palaeoclimatol. Palaeoecol. 170, 11–26.

Guo, Z.T., Ruddiman, W.F., Hao, Q.Z., Wu, H.B., Qiao, Y.S., Zhu, R.X., Peng, S.Z., Wei, J.J., Yuan, B.Y., Liu, T.S., 2002. Onset of Asian desertification by 22 Myr ago inferred from loess deposits in China. Nature 416, 159–163.

Hao, Q.Z., Guo, Z.T., 2004. Magnetostratigraphy of a late Miocene-Pliocene loess-soil sequence in the western Loess Plateau in China. Geophys. Res. Lett. 31, L09209. https://doi.org/10.1029/2003GL019392.

Hovan, S.A., Rea, D.K., Pisias, N.G., Shackleton, N.J., 1989. A direct link between the China loess and marine δ18O records: aeolian flux to the north Pacific. Nature 340, 296–298.

Howard, J.L., 1992. An evaluation of shape indices as palaeoenvironmental indicators using quartzite and metavolcanic clasts in Upper Cretaceous to Palaeogene beach, river and submarine fan conglomerates. Sedimentology 39:471–486. https://doi.org/10.1111/j.1365-3091.1992.tb02128.x.

Jonkers, L., Prins, M.A., Brummer, G.-J.A., Konert, M., Lougheed, B.C., 2009. Experimental insights into laser diffraction particle sizing of fine-grained sediments for use in palaeoceanography. Sedimentology 56:2192–2206. https://doi.org/10.1111/j.1365-3091.2009.01076.x.

Jonkers, L., Barker, S., Hall, I.R., Prins, M.A., 2015. Correcting for the influence of ice-rafted detritus on grain size-based paleocurrent speed estimates. Paleoceanography 30: 1347–1357. https://doi.org/10.1002/2015PA002830.

Kaakinen, A., Lunkka, J.P., 2003. Sedimentation of the Late Miocene Bahe Formation and its implications for stable environments adjacent to Qinling Mountains in Shaanxi, China. J. Asian Earth Sci. 22, 67–78.

Kaakinen, A., Passey, B.H., Zhang, Z., Liu, L., Pesonen, L.J., Fortelius, M., 2013. Stratigraphy and paleoecology of the classical dragon bone localities of Baode County, Shanxi Province. In: Wang, X., Flynn, L.J., Fortelius, M. (Eds.), Fossil Mammals of Asia: Neogene Biostratigraphy and Chronology. Columbia University Press, New York, pp. 203–217.

Kohfeld, K., 2003. Glacial-interglacial changes in dust deposition on the Chinese Loess Plateau. Quat. Sci. Rev. 22, 1859–1878.

Konert, M., Vandenberghe, J., 1997. Comparison of laser grain size analysis with pipette and sieve analysis: a solution for the underestimation of the clay fraction. Sedimentology 44:523–535. https://doi.org/10.1046/j.1365-3091.1997.d01-38.x.

Krumbein, W.C., 1941. Measurement and geological significance of shape and roundness of sedimentary particles. J. Sediment. Res. 11:64–72. https://doi.org/10.1306/D42690F3-2B26-11D7-8648000102C1865D.

Kukla, G., 1987. Loess stratigraphy in central China. Quat. Sci. Rev. 6, 191–219.

Kwan, A.K.H., Mora, C.F., Chan, H.C., 1999. Particle shape analysis of coarse aggregate using digital image processing. Cem. Concr. Res. 29, 1403–1410.

Li, D., Kang, Y., Li, D., 2015. Comparison of grain-size and grain-shape characters of alluvial and lakeshore sands based on dynamic image analysis. Quat. Sci. 35, 484–492 (in Chinese with English abstract).

Licht, A., Pullen, A., Kapp, P., Abell, J., Giesler, N., 2016. Eolian cannibalism: reworked loess and fluvial sediment as the main sources of the Chinese Loess Plateau. Geol. Soc. Am. Bull. 128:1–13. https://doi.org/10.1130/B31375.1.
Lisiecki, L.E., Raymo, M.E., 2005. A Pliocene-Pleistocene stack of 57 globally distributed benthic $\delta^{18}O$ records. Paleoceanography 20, PA1003. https://doi.org/10.1029/2004PA001071.
Liu, T.S., 1985. Loess and the Environment. China Ocean Press, Beijing.
Liu, T., Ding, Z., 1998. Chinese Loess and the Paleomonsoon. Annu. Rev. Earth Planet. Sci. 26:111–145. https://doi.org/10.1146/annurev.earth.26.1.111.
Lu, H.Y., Sun, D.H., 2000. Pathways of dust input to the Chinese Loess Plateau during the last glacial and interglacial periods. Catena 40, 251–261.
Lu, H.Y., Vandenberghe, J., An, Z.S., 2001. Aeolian origin and palaeoclimatic implications of the 'Red Clay' (north China) as evidenced by grain-size distribution. J. Quat. Sci. 16, 89–97.
Mazzullo, J., Alexander, A., Tieh, T., Ding, M., 1992. The effects of wind transport on the shapes of quartz silt grains. J. Sediment. Petrol. 62:961–971. https://doi.org/10.1306/D4267A28-2B26-11D7-8648000102C1865D.
Mclaren, P., Bowles, D., 1985. The effects of sediments transport on grain-size distributions. J. Sediment. Res. 55, 457–470.
Miao, X., Sun, Y., Lu, H., Mason, J.A., 2004. Spatial pattern of grain size in the Late Pliocene 'Red Clay' deposits (North China) indicates transport by low-level northerly winds. Palaeogeogr. Palaeoclimatol. Palaeoecol. 206, 149–155.
Muhs, D.R., 2013. The geologic records of dust in the Quaternary. Aeolian Res. 9, 3–48.
Nalluri, V.R., Schirg, P., Gao, X., Virdis, A., Imanidis, G., Kuentz, M., 2010. Different modes of dynamic image analysis in monitoring of pharmaceutical dry milling process. Int. J. Pharm. 391, 107–114.
Nie, J., Stevens, T., Rittner, M., Stockli, D., Garzanti, E., Limonta, M., Bird, A., Ando, S., Vermeesch, P., Saylor, J., Lu, H., Breecker, D., Hu, X., Liu, S., Resentini, A., Vezzoli, G., Peng, W., Carter, A., Ji, S., Pan, B., 2015. Loess Plateau storage of Northeastern Tibetan Plateau-derived Yellow River sediment. Nat. Commun. 6:8511. https://doi.org/10.1038/ncomms9511.
Nie, J., Song, Y., King, J.W., 2016. A review of recent advances in red-clay environmental magnetism and paleoclimate history on the Chinese Loess Plateau. Front. Earth Sci. 4. https://doi.org/10.3389/feart.2016.00027.
Nugteren, G., Vandenberghe, J., 2004. Spatial climatic variability on the Central Loess Plateau (China) as recorded by grain size for the last 250 kyr. Glob. Planet. Chang. 41, 185–206.
Oakey, R.J., Green, M., Carling, P.A., Lee, M.W.E., Sear, D.A., Warburton, J., 2005. Grain-shape analysis—a new method for determining representative particle shapes for populations of natural grains. J. Sediment. Res. 75:1065–1073. https://doi.org/10.2110/jsr.2005.079.
Persson, A.-L., 1998. Image analysis of shape and size of fine aggregates. Eng. Geol. 50, 177–186.
Porter, S.C., 2001. Chinese loess record of monsoon climate during the last glacial–interglacial cycle. Earth Sci. Rev. 54, 115–128.
Prins, M.A., Vriend, M., 2007. Glacial and interglacial eolian dust dispersal patterns across the Chinese Loess Plateau inferred from decomposed loess grain-size records. Geochem. Geophys. Geosyst. 8, Q07Q05. https://doi.org/10.1029/2006GC001563.
Prins, M.A., Weltje, G.J., 1999. End-member modeling of siliciclastic grain-size distributions: the Late Quaternary record of eolian and fluvial sediment supply to the Arabian Sea and its paleoclimatic significance. In: Harbaugh, J., Watney, L., Rankey, G., Slingerland, R., Goldstein, R., Franseen, E. (Eds.), Numerical Experiments in Stratigraphy: Recent Advances in Stratigraphic and Sedimentologic Computer Simulations. SEPM Society for Sedimentary Geology, pp. 91–111.
Prins, M.A., Postma, G., Weltje, G.J., 2000. Controls on terrigenous sediment supply to the Arabian Sea during the late Quaternary: the Makran continental slope. Mar. Geol. 169, 351–371.
Prins, M.A., Vriend, M., Nugteren, G., Vandenberghe, J., Lu, H., Zheng, H., Jan Weltje, G., 2007. Late Quaternary aeolian dust input variability on the Chinese Loess Plateau: inferences from unmixing of loess grain-size records. Quat. Sci. Rev. 26, 230–242.
Prins, M.A., Zheng, H., Beets, C.J., Troelstra, S.R., Bacon, P., Kamerling, I.M., Wester, W., Konert, M., Huang, X., Wang, X., Vandenberghe, J., 2009. Dust supply from river floodplains: the case of the lower Huang He (Yellow River) recorded in a loess-palaeosol sequence from the Mangshan Plateau. J. Quat. Sci. 24, 75–84.
Pye, K., 1994. Shape sorting during wind transport of quartz silt grains - discussion. J. Sediment. Res. 64:704–705. https://doi.org/10.1306/D4267E8D-2B26-11D7-8648000102C1865D.
Pye, K., 1995. The nature, origin and accumulation of loess. Quat. Sci. Rev. 14:653–667. https://doi.org/10.1016/0277-3791(95)00047-X.
Rea, D.K., Hovan, S.A., 1995. Grain size distribution and depositional processes of the mineral component of abyssal sediments: lessons from the North Pacific. Paleoceanography 10:251–258. https://doi.org/10.1029/94PA03355.
Riley, N.A., 1941. Projection Sphericity. J. Sediment. Res. 11:94–97. https://doi.org/10.1306/D426910C-2B26-11D7-8648000102C1865D.
Rodriguez, J.M., Edeskär, T., Knutsson, S., 2013. Particle shape quantities and measurement techniques: an overview. Electron. J. Geotech. Eng. 18, 169–198.
Shang, Y., Beets, C.J., Tang, H., Prins, M.A., Lahaye, Y., van Elsas, R., Sukselainen, L., Kaakinen, A., 2016. Variations in the provenance of the late Neogene Red Clay deposits in northern China. Earth Planet. Sci. Lett. 439, 88–100.
Sneed, E.D., Folk, R.L., 1958. Pebbles in the lower Colorado River, Texas a study in particle morphogenesis. J. Geol. 66, 114–150.
Stevens, T., Carter, A., Watson, T.P., Vermeesch, P., Andò, S., Bird, A.F., Lu, H., Garzanti, E., Cottam, M.A., Sevastjanova, I., 2013. Genetic linkage between the Yellow River, the Mu Us desert and the Chinese Loess Plateau. Quat. Sci. Rev. 78, 355–368.
Stuut, J.-B.W., Prins, M.A., Schneider, R.R., Weltje, G.J., Jansen, J.H.F., Postma, G., 2002. A 300-kyr record of aridity and wind strength in southwestern Africa: inferences from grain-size distributions of sediments on Walvis Ridge, SE Atlantic. Mar. Geol. 180, 221–233.
Stuut, J.-B.W., Temmesfeld, F., De Deckker, P., 2014. A 550 ka record of aeolian activity near North West Cape, Australia: inferences from grain-size distributions and bulk chemistry of SE Indian Ocean deep-sea sediments. Quat. Sci. Rev. 83, 83–94.
Sun, D., Bloemendal, J., Rea, D.K., Vandenberghe, J., Jiang, F., An, Z., Su, R., 2002. Grain-size distribution function of polymodal sediments in hydraulic and aeolian environments, and numerical partitioning of the sedimentary components. Sediment. Geol. 152, 263–277.
Sun, D., Bloemendal, J., Rea, D.K., An, Z., Vandenberghe, J., Lu, H., Su, R., Liu, T., 2004. Bimodal grain-size distribution of Chinese loess, and its palaeoclimatic implications. Catena 55, 325–340.
Suzuki, K., Fujiwara, H., Ohta, T., 2015. The evaluation of macroscopic and microscopic textures of sand grains using elliptic Fourier and principal component analysis: implications for the discrimination of sedimentary environments. Sedimentology 62: 1184–1197. https://doi.org/10.1111/sed.12183.
Syvitski, J.P.M., 1997. Principles, Methods, and Application of Particles Size Analysis. Cambridge University Press, Cambridge.
Tysmans, D., Claeys, P., Deriemaeker, L., Maes, D., Finsy, R., Van Molle, M., 2006. Size and shape analysis of sedimentary grains by automated dynamic image analysis. Part. Part. Syst. Charact. 23:381–387. https://doi.org/10.1002/ppsc.200500965.
Tysmans, D., Haesaerts, P., Bogemans, F., Claeys, P., Finsy, R., Van Molle, M., 2009. Heterogeneity in homogeneous Brabantian loess during the Late Pleniglacial. Quat. Int. 198, 195–203.
Udden, J.A., 1914. Mechanical composition of clastic sediments. Bull. Geol. Soc. Am. 25: 655–744. https://doi.org/10.1130/GSAB-25-655.
Újvári, G., Kok, J.F., Varga, G., Kovács, J., 2016. The physics of wind-blown loess: implications for grain size proxy interpretations in Quaternary paleoclimate studies. Earth Sci. Rev. 154, 247–278.
Vandenberghe, J., 2013. Grain size of fine-grained windblown sediment: a powerful proxy for process identification. Earth Sci. Rev. 121, 18–30.
Vandenberghe, J., Lu, H.Y., Sun, D.H., van Huissteden, J., Konert, M., 2004. The late Miocene and Pliocene climate in East Asia as recorded by grain size and magnetic susceptibility of the Red Clay deposits (Chinese Loess Plateau). Palaeogeogr. Palaeoclimatol. Palaeoecol. 204, 239–255.
Visher, G.S., 1969. Grain size distributions and depositional processes. J. Sediment. Res. 39, 1074–1106.
Vriend, M., Prins, M.A., Buylaert, J.P., Vandenberghe, J., Lu, H.Y., 2011. Contrasting dust supply patterns across the north-western Chinese Loess Plateau during the last glacial-interglacial cycle. Quat. Int. 240, 167–180.
Wadell, H., 1932. Volume, shape, and roundness of rock particles. J. Geol. 40, 443–451.
Wadell, H., 1935. Volume, shape, and roundness of quartz particles. J. Geol. 43, 250–280.
Weltje, G.J., 1997. End-member modeling of compositional data: numerical-statistical algorithms for solving the explicit mixing problem. Math. Geol. 29, 503–549.
Weltje, G.J., Prins, M.A., 2003. Muddled or mixed? Inferring paleoclimate from size distributions of deep-sea clastics. Sediment. Geol. 162, 39–62.
Weltje, G.J., Prins, M.A., 2007. Genetically meaningful decomposition of grain-size distributions. Sediment. Geol. 202, 409–424.
Wen, L.J., Lu, H.Y., Qiang, X.K., 2005. Changes in grain-size and sedimentation rate of the Neogene Red Clay deposits along the Chinese Loess Plateau and implications for the palaeowind system. Sci. China Ser. D Earth Sci. 48:1452–1462. https://doi.org/10.1360/01yd0558.
Wentworth, C.K., 1922. A scale of grade and class terms for clastic sediments. J. Geol. 30, 377–392.
Xiao, J., Chang, Z., Si, B., Qin, X., Itoh, S., Lomtatidze, Z., 2009. Partitioning of the grain-size components of Dali Lake core sediments: evidence for lake-level changes during the Holocene. J. Paleolimnol. 42, 249–260.
Xiao, G.Q., Zong, K.Q., Li, G.J., Hu, Z.C., Dupont-Nivet, G., Peng, S.Z., Zhang, K.X., 2012. Spatial and glacial-interglacial variations in provenance of the Chinese Loess Plateau. Geophys. Res. Lett. 39, L20715. https://doi.org/10.1029/2012GL053304.
Xiao, J., Fan, J., Zhou, L., Zhai, D., Wen, R., Qin, X., 2013. A model for linking grain-size component to lake level status of a modern clastic lake. J. Asian Earth Sci. 69, 149–158.
Yang, S.L., Ding, Z.L., 2004. Comparison of particle size characteristics of the Tertiary 'red clay' and Pleistocene loess in the Chinese Loess Plateau: implications for origin and sources of the 'red clay'. Sedimentology 51:77–93. https://doi.org/10.1046/j.1365-3091.2003.00612.x.
Yu, W., Hancock, B.C., 2008. Evaluation of dynamic image analysis for characterizing pharmaceutical excipient particles. Int. J. Pharm. 361, 150–157.
Yu, W., Muteki, K., Zhang, L., Kim, G., 2011. Prediction of bulk powder flow performance using comprehensive particle size and particle shape distributions. J. Pharm. Sci. 100:284–293. https://doi.org/10.1002/jps.22254.
Zhang, Z.Q., Kaakinen, A., Liu, L.P., Lunkka, J.P., Sen, S., Gose, W.A., Qiu, Z.D., Zheng, S.H., Fortelius, M., 2013. Mammalian biochronology of the late Miocene Bahe Formation. In: Wang, X.M., Flynn, L.J., Fortelius, M. (Eds.), Fossil Mammals of Asia: Neogene Biostratigraphy 1062 and Chronology. Columbia University Press, New York, pp. 187–202.
Zhu, Y., Zhou, L., Mo, D., Kaakinen, A., Zhang, Z., Fortelius, M., 2008. A new magnetostratigraphic framework for late Neogene Hipparion Red Clay in the eastern Loess Plateau of China. Palaeogeogr. Palaeoclimatol. Palaeoecol. 268, 47–57.